Peer-reviewed version available at *plasma* **2018**, *1*, 10; doi:10.3390/plasma1010010

Article

Fully kinetic simulation of ion-temperature-gradient instability in tokamaks

Youjun Hu [1,2], Matthew T. Miecnikowski [1], Yang Chen[1] and Scott E. Parker [1,*]

[1] Department of Physics, University of Colorado, Boulder, Colorado 80309, USA; youjun.hu@colorado.edu
[2] Institute of Plasma Physics, Chinese Academy of Sciences, Hefei, Anhui 230031, China
* Correspondence: sparker@colorado.edu

Abstract: The feasibility of using full ion kinetics, instead of gyrokinetics, in simulating low-frequency Ion-Temperature-Gradient (ITG) instabilities in tokamaks has recently been demonstrated by Sturdevant et al. [*Physics of Plasmas* **24**, 081207 (2017)]. In that work, a variational integrator was developed to integrate the full orbits of ions in toroidal geometry, which proved to be accurate in capturing both the short-time scale cyclotron motion and long time scale drift motion. The present work extends that work in three aspects. First, we implement a relatively simple full orbit integrator, the Boris integrator, and demonstrate that the accuracy of this integrator is also sufficient for simulation of ITG instabilities. Second, the equilibrium magnetic configuration is extended to general toroidal configuration specified numerically, enabling simulation of realistic equilibria reconstructed from tokamak experiments. Third, we extend that work to the nonlinear regime and investigate the nonlinear saturation of ITG instabilities. To verify the new numerical implementation of the orbit integrator and magnetic configuration, the linear electrostatic ITG frequency and growth rate are compared with those given in Sturdevant's work and good agreement is found.

Keywords: fully kinetic ions; ion temperature gradient instabilities; tokamak; gyrokinetics; particle-in-cell

1. Introduction

Ion temperature gradients in tokamaks provide free energy to micro-instabilities called Ion-Temperature-Gradient (ITG) instabilities[1]. The nonlinear development of these instabilities, i.e., ITG turbulence, is believed to play an important role in regulating particle and heat transport in tokamaks[2–4]. There are numerous papers devoted to the gyrokinetic simulation of ITG turbulence, which employ gyrokinetic theory to decouple the high-frequency gyro-motion of ions from the low-frequency ITG modes[5–10]. However, gyrokinetics rely on ordering assumptions in deriving the gyrokinetic equation. One of these ordering assumptions, $\rho_i/L_n \ll 1$, becomes questionable in tokamak edge with steep density profile, where ρ_i is the gyro-radius of ions and L_n is the scale length of density profile. For this reason, tokamak edge gyrokinetic codes, e.g. XGC[11,12], are usually limited in the regime where the pedestal width is much greater than the ion gyro-radius. Fully kinetic ion models[13–16], which retain the ion gyro-motion, avoid these problematic ordering assumptions (although involving more computations in simulations). Low-frequency full kinetics have already been demonstrated in slab geometry[17], successfully benchmarked against gyrokinetics for the slab ITG[18], and extended to toroidal ITG instabilities by Sturdevant et al.[19]. In the latter work, a variational integrator was developed to integrate the full orbits of ions in toroidal geometry, which proved to be accurate in capturing both the short-time scale cyclotron motion and long time scale drift motion. However the variational integrator requires solution of a nonlinear equation at each time step, requiring extra computational time. Another limitation of that work is that the equilibrium magnetic field is specified analytically and restricted to circular flux surface configurations.

Peer-reviewed version available at *plasma* **2018**, *1*, 10; doi:10.3390/plasma1010010

The present work extends that work in three aspects. First, we implement a simpler full orbit integrator, the Boris integrator[20], in toroidal geometry and demonstrate that the accuracy of this integrator is also sufficient for simulation of ITG instabilities. Second, the equilibrium magnetic configuration is extended to general toroidal configuration specified numerically, enabling simulation of realistic equilibria reconstructed from tokamak experiments. Third, we extend the work in Ref. [19] to the nonlinear regime and investigate the nonlinear saturation of ITG instabilities. To verify the new numerical implementation of the orbit integrator and magnetic configuration, the linear electrostatic ITG frequency and growth rate are compared with those given in Ref. [19] and good agreement is found. The simulation adopts the δf particle-in-cell (PIC) method. The δf method is chosen because it is good at resolving perturbations with low amplitude. The PIC method is chosen because it samples the phase-space by the using Monte-Carlo method and the accuracy of the resulting Monte-Carlo integration is superior to the continuum method as dimensionality increases (six dimensional in this work).

The remainder of the paper is organized as follows. Section 2 discusses the fully kinetic ion model for simulating ITG instabilities. The implicit δf PIC method and the full orbit integrator are briefly discussed in Sec. 3. Section 4 discusses how magnetic configuration and magnetic coordinates are handled in our numerical model. Section 5 gives the linear and nonlinear simulation results of ITG instabilities and the linear benchmark against the results of Ref. [19]. A brief summary is given in Sec. 6. Appendix A discusses the electromagnetic model we are working on.

2. Fully kinetic ion model of ITG instabilities

The fully kinetic ion model for ITG instabilities is described in Ref. [19]. The following is a summary of the model. The ion Vlasov equation is written

$$\frac{df_i}{dt} \equiv \frac{\partial f_i}{\partial t} + \mathbf{v} \cdot \frac{\partial f_i}{\partial \mathbf{x}} + \frac{q_i}{m_i}(\mathbf{E} + \mathbf{v} \times \mathbf{B}) \cdot \frac{\partial f_i}{\partial \mathbf{v}} = 0, \tag{1}$$

where $f_i(\mathbf{x}, \mathbf{v})$ is the ion distribution function, $\mathbf{x}$ and $\mathbf{v}$ are ion position and velocity respectively, $\mathbf{E}$ and $\mathbf{B}$ are the electric field and magnetic field respectively, q_i and m_i are the charge and mass of ions respectively. We write f_i as an equilibrium part plus a perturbation, i.e., $f_i = f_{i0} + \delta f_i$, then Eq. (1) is written as

$$\frac{d\delta f_i}{dt} = -\frac{q_i}{m_i}(\delta\mathbf{E} + \mathbf{v} \times \delta\mathbf{B}) \cdot \frac{\partial f_{i0}}{\partial \mathbf{v}}, \tag{2}$$

where $\delta\mathbf{E}$ and $\delta\mathbf{B}$ are the perturbed part of the electric field and magnetic field, respectively.

To model ITG instabilities, the equilibrium part of ion distribution function f_{i0} is chosen as[19]

$$f_{i0}(R_r, v) = n_{i0}(R_r)\left(\frac{m_i}{2\pi T_{i0}(R_r)}\right)^{3/2} \exp\left[-\frac{m_i v^2}{2T_{i0}(R_r)}\right], \tag{3}$$

where n_{i0} and T_{i0} are ion number density and temperature, which depend on a radial variable R_r given by

$$R_r = r + \frac{m_i}{q_i}\frac{\mathbf{v} \times \mathbf{b}}{B_0} \cdot \nabla r, \tag{4}$$

where r is the minor radius of magnetic surfaces and $\mathbf{b} = \mathbf{B}_0/B_0$ is the unit vector along the equilibrium magnetic field $\mathbf{B}_0$. The variable R_r is a radial coordinate of the ion guiding-center and thus an approximate constant of motion in the weakly inhomogeneous tokamak magnetic field with $\rho_i/L_B \ll 1$, where L_B is the scale length of $\mathbf{B}_0$. Since arbitrary functions of the constants of motion are solutions to the kinetic equation, the distribution function given by Eq. (3) is approximately an

Peer-reviewed version available at plasma 2018, 1, 10; doi:10.3390/plasma1010010

equilibrium solution to the kinetic equation (1). Using this form of equilibrium distribution, the kinetic equation (2) for the perturbed part of the distribution is written as

$$\begin{aligned} \frac{d\delta f_i}{dt} &= \frac{q_i}{T_i} f_{i0} \delta \mathbf{E} \cdot \mathbf{v} + \left[\kappa_{n_i} + \left(\frac{mv^2}{2T_i} - \frac{3}{2} \right) \kappa_{T_i} \right] f_{i0} \frac{(\delta \mathbf{E} \times \mathbf{b}) \cdot \nabla r}{B_0} \\ &- \left[\kappa_{n_i} + \left(\frac{mv^2}{2T_i} - \frac{3}{2} \right) \kappa_{T_i} \right] f_{i0} (\mathbf{v} \times \delta \mathbf{B}) \cdot \frac{\nabla r \times \mathbf{b}}{B_0}, \end{aligned} \tag{5}$$

where $\kappa_{n_i} = -n_{i0}^{-1} \partial n_{i0} / \partial R_r$ and $\kappa_{T_i} = -T_{i0}^{-1} \partial T_{i0} / \partial R_r$ are the radial gradients of ion density and temperature, respectively.

2.1. Electrostatic limit with adiabatic electrons

In this work, we focus on the electrostatic limit, in which $\delta \mathbf{B}$ is zero and $\delta \mathbf{E} = -\nabla \delta \Phi$, where $\delta \Phi$ is the perturbed electric potential. Furthermore, we adopt the simple adiabatic electron model for describing the electron response, in which the perturbed electron density is related to $\delta \Phi$ by

$$\delta n_e = n_{e0} \frac{e(\delta \Phi - \langle \delta \Phi \rangle)}{T_{e0}}, \tag{6}$$

where n_{e0} and T_{e0} are the equilibrium electron number density and temperature, respectively; e is the elementary charge, $\langle \ldots \rangle$ is the magnetic surface averaging operator defined by

$$\langle \ldots \rangle = \frac{\int_0^{2\pi} \int_{-\pi}^{+\pi} (\ldots) \mathcal{J} d\phi d\theta}{\int_0^{2\pi} \int_{-\pi}^{+\pi} \mathcal{J} d\phi d\theta}, \tag{7}$$

where $\mathcal{J}$ is the Jacobian of magnetic coordinates (ψ, θ, ϕ), ψ is a radial coordinate, θ and ϕ are poloidal and toroidal angles, respectively.

In the electrostatic limit, Maxwell's equations reduce to Poisson's equation, which further reduces to the quasi-neutrality condition if the space-charge term is neglected. The quasi-neutrality condition is written as

$$\delta n_e = \delta n_i \tag{8}$$

where δn_i is the perturbed part of the ion number density. Using δn_e given by Eq. (6) in the above equation, we obtain

$$n_{e0} \frac{e(\delta \Phi - \langle \delta \Phi \rangle)}{T_e} = \delta n_i, \tag{9}$$

which serves as our field equation, from which the electric potential $\delta \Phi$ can be solved. We consider modes with $n \neq 0$, where n is the toroidal mode number. Then the flux average $\langle \delta \Phi \rangle$ is always zero and the field equation (9) reduces to an algebraic equation, which can be analytically solved to give

$$\delta \Phi = \frac{T_e}{e} \frac{\delta n_i}{n_{e0}}. \tag{10}$$

We are working on extending the fully kinetic ion model for ITG instabilities to the electromagnetic case with drift-kinetic electrons. This model is discussed in Appendix A.

3. Implicit δf particle-in-cell method and full orbit integrator

The ion Vlasov equation (5) is solved by using the δf PIC method[21,22], in which an assembly of markers are loaded in the phase-space according to a distribution function $g(\mathbf{x}, \mathbf{v})$. Then the phase space volume occupied by a marker located at $(\mathbf{x}_j, \mathbf{v}_j)$ is given by $V_{\mathrm{ps}\,j} = 1/g(\mathbf{x}_j, \mathbf{v}_j)$. We define the weight of the j th marker by

Peer-reviewed version available at *plasma* **2018**, *1*, 10; doi:10.3390/plasma1010010

$$w_{ij} = \delta f_i(\mathbf{x}_j, \mathbf{v}_j) V_{\mathrm{ps}\,j} = \frac{\delta f_i(\mathbf{x}_j, \mathbf{v}_j)}{g(\mathbf{x}_j, \mathbf{v}_j)}, \tag{11}$$

which is the physical particle number carried by δf_i in the phase space volume $V_{\mathrm{ps}\,j}$. The weight evolution equation is obtained by multiplying both sides of Eq. (5) by $V_{\mathrm{ps}\,j}$ and noting that $d(V_{\mathrm{ps}\,j})/dt = 0$, yielding

$$\begin{aligned} \frac{dw_{ij}}{dt} &= \frac{f_{i0}}{g}\frac{q_i}{T_i}\delta\mathbf{E}\cdot\mathbf{v} \\ &+ \frac{f_{i0}}{g}\left[\kappa_{n_i} + \left(\frac{mv^2}{2T_i} - \frac{3}{2}\right)\kappa_{T_i}\right]\frac{(\delta\mathbf{E}\times\mathbf{b})\cdot\nabla r}{B_0}, \end{aligned} \tag{12}$$

where the magnetic perturbation terms have been dropped due to the electrostatic approximation. An implicit scheme is used to integrate the weight evolution equation. Denoting the right-hand side of the weight evolution equation (12) by $h(\delta\mathbf{E}, \mathbf{x}, \mathbf{v})$, the implicit scheme we use takes the following form:

$$\frac{w_{ij}^{(n+1)} - w_{ij}^{(n)}}{\Delta t} = h(\delta\mathbf{E}^{(n+1/2)}, \mathbf{x}_j^{(n+1/2)}, \mathbf{v}_j^{(n+1/2)}), \tag{13}$$

with

$$\delta\mathbf{E}^{(n+1/2)} = \frac{\delta\mathbf{E}^{(n+1)} + \delta\mathbf{E}^{(n)}}{2}, \tag{14}$$

We choose the initial guess of $\delta\mathbf{E}^{(n+1)}$ to be equal to $\delta\mathbf{E}^{(n)}$ and then iterate until convergence is achieved. If the iteration is terminated after only two iterations, then this scheme corresponds to the predictor-corrector scheme called Heun's method[23]. The field equation (9) needs to be solved once in each iteration.

The ion trajectory $(\mathbf{x}_j, \mathbf{v}_j)$ is advanced by a time-centered difference scheme given by

$$\frac{\mathbf{v}^{(n+1/2)} - \mathbf{v}^{(n-1/2)}}{\Delta t} = \frac{q_i}{m_i}\left[\mathbf{E}^{(n)}(\mathbf{x}^{(n)}) + \frac{\mathbf{v}^{(n+1/2)} + \mathbf{v}^{(n-1/2)}}{2} \times \mathbf{B}^{(n)}(\mathbf{x}^{(n)})\right]. \tag{15}$$

for velocity and

$$\frac{\mathbf{x}^{(n+1)} - \mathbf{x}^{(n)}}{\Delta t} = \mathbf{v}^{(n+1/2)}, \tag{16}$$

for position. Here "staggered" time grids are used for $\mathbf{v}$ and $\mathbf{x}$: time grids of $\mathbf{v}$ are at half-steps while time grids of $\mathbf{x}$ are at integer steps. The position at half-steps, $\mathbf{x}^{(n+1/2)}$, which is needed in Eq. (13), is approximated by $\mathbf{x}^{(n+1/2)} = (\mathbf{x}^{(n)} + \mathbf{x}^{(n+1)})/2$. Further note that the scheme given in Eq (15) is in an implicit form since the unknown $\mathbf{v}^{(n+1/2)}$ appears on both sides of the equation. Fortunately, equation (15) can be analytically solved in Cartesian basis and its explicit solution is expressed by the Boris algorithm[20]. As is discussed in Ref. [24], the above scheme conserves the phase-space volume, which makes it suitable for particle-based methods where phase-space volume conservation is usually implicitly assumed. In this work, cylindrical coordinates are used in integrating the ion orbits. When implementing the Boris scheme in cylindrical coordinates, a local Cartesian coordinate system with basis vectors $(\mathbf{e}_x, \mathbf{e}_y, \mathbf{e}_z)$ along the local cylindrical basis vectors $(\mathbf{e}_R, \mathbf{e}_\phi, \mathbf{e}_Z)$ at particle location $\mathbf{x}^{(n)}$ is set up to perform the velocity integration to obtain $\mathbf{v}^{(n+1/2)}$. Then the particle location is updated in the local Cartesian coordinates by using Eq. (16) and then is transformed to the cylindrical coordinates by using the analytic coordinate transformation. After this, the new velocity $\mathbf{v}^{(n+1/2)}$ is projected onto the new basis vectors $(\mathbf{e}_R, \mathbf{e}_\phi, \mathbf{e}_Z)$ at particle location $\mathbf{x}^{(n+1)}$. Typical full ion orbits computed by this scheme are compared with the guiding center orbit in Figure 1. This scheme can reproduce correct

Peer-reviewed version available at *plasma* **2018**, *1*, 10; doi:10.3390/plasma1010010

drift motion even when a large time-step comparable to the gyro-period is used[25]. Figure 1 shows examples of orbits computed with large time steps.

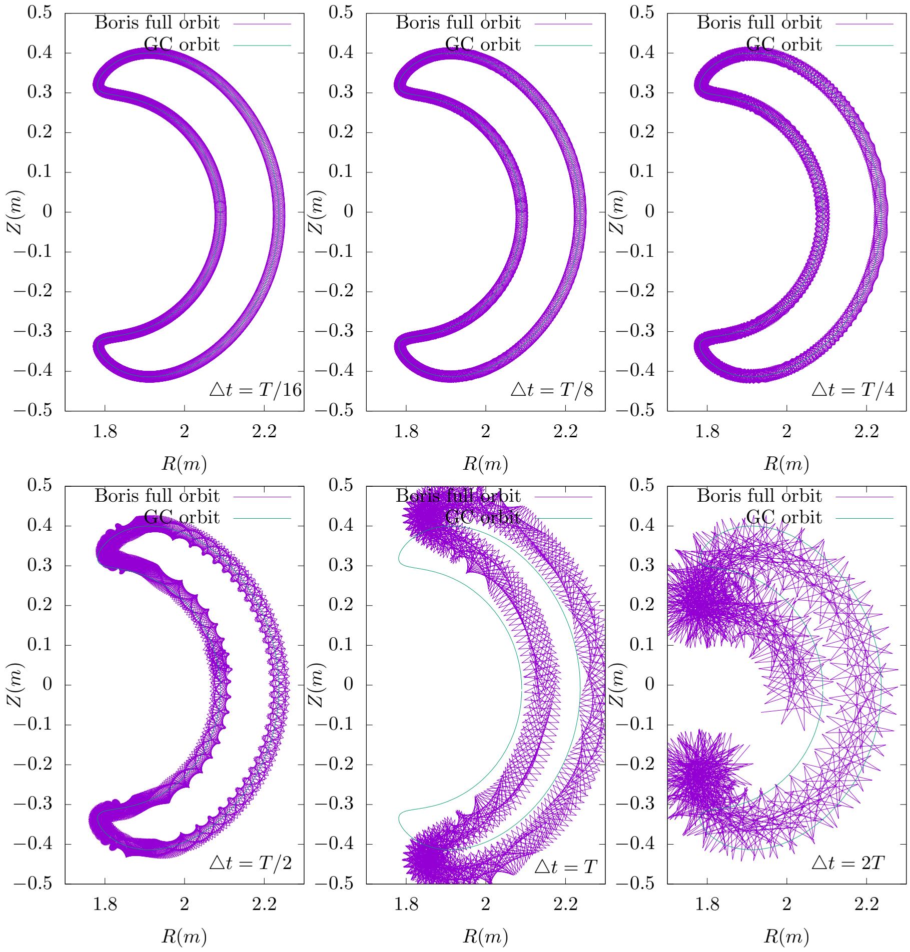

Figure 1. Comparison between the full orbits calculated by the Boris scheme with different time step sizes: $\Delta t = T/16$, $\Delta t = T/8$, $\Delta t = T/4$, $\Delta t = T/2$, $\Delta t = T$, and $\Delta t = 2T$, where T is the ion (Deuteron) gyro-period at its initial location ($R = 2.1m$, $Z = 0m$, $\phi = 0$). The results show that the full orbits agrees with the guiding-center orbit for the cases with time-step $\Delta t < T/4$. When Δt is further increased, the computed full orbits deviate from the guiding-center orbit. Further note that the gyro-radius obtained remains nearly the same when the time-step $\Delta t < T/4$. When Δt is further increased, the gyro-radius becomes larger than the correct value. The magnetic configuration is from EAST tokamak discharge#59954@3.03s. The initial velocity is given by $v_R = v_Z = 1.0 \times 10^6 m/s$, and $v_\phi = 5 \times 10^5 m/s$, which corresponds to a kinetic energy of 23 keV. For $\Delta t = T/16$, the orbit is advanced by 23250 time-steps, in which the particle finishes one banana period.

In the linear limit, the fields $\mathbf{E}$ and $\mathbf{B}$ on the right-hand side of Eq (15) are replaced by the equilibrium fields $\mathbf{E}_0$ and $\mathbf{B}_0$. In the present work, $\mathbf{E}_0 = 0$ and $\mathbf{B}_0$ is a general toroidal magnetic configuration specified numerically.

4. Magnetic field specification and field-line-following coordinates

The equilibrium magnetic field is specified numerically by reading and interpolating the output of the equilibrium reconstruction code EFIT[26]. This enables us to handle magnetic configurations with arbitrary flux surface shape.

A field-line-following coordinate system[27,28] (ψ, θ, α) is constructed from the numerical magnetic configuration, with the radial coordinate ψ being the normalized poloidal magnetic

Peer-reviewed version available at *plasma* **2018**, *1*, 10; doi:10.3390/plasma1010010

flux, θ being an equal-volume poloidal angle and α being a generalized toroidal angle defined by $\alpha = \phi - \int_0^\theta \hat{q} d\theta$, where ϕ is the cylindrical toroidal angle, and $\hat{q} = \mathbf{B} \cdot \nabla\phi / \mathbf{B} \cdot \nabla\theta$ is the local safety factor. In (ψ, θ, α) coordinate system, both $\nabla\psi$ and $\nabla\alpha$ are perpendicular the field lines, i.e. $\mathbf{B}_0 \cdot \nabla\psi = 0$, and $\mathbf{B}_0 \cdot \nabla\alpha = 0$. Furthermore the gradient along the field line is written as

$$\mathbf{B}_0 \cdot \nabla = -\Psi' \mathcal{J}^{-1} \frac{\partial}{\partial\theta}, \tag{17}$$

where $\Psi' = d\Psi/d\psi$ with $\Psi = A_\phi R$ the poloidal magnetic flux function, and $\mathcal{J} = (\nabla\psi \times \nabla\theta \cdot \nabla\alpha)^{-1}$ is the Jacobian of the (ψ, θ, α) coordinates.

Ion markers are loaded in the field-line-following coordinates (ψ, θ, α). Ion trajectories are integrated in cylindrical coordinates (R, ϕ, Z) and then linearly interpolated to (ψ, θ, α) coordinates to do the deposition in order to obtain the perturbed ion density at the spatial grids of (ψ, θ, α) coordinates. At a grid point $\mathbf{x}_k$, the perturbed ion density is approximated by

$$\delta n_i(\mathbf{x}_k) = \frac{1}{\Delta V_s} \sum_{j=1}^{N_p} w_{ij} S(\mathbf{x}_k - \mathbf{x}_j), \tag{18}$$

where N_p is the total number of markers loaded, $\Delta V_s = \mathcal{J}(\mathbf{x}_k)\Delta\psi\Delta\theta\Delta\alpha$ is the volume of the spatial cell, $\Delta\psi$, $\Delta\theta$, and $\Delta\alpha$ are the grid point spacings in the ψ, θ and α direction respectively, S is the interpolating function defined as

$$S(\mathbf{x}) = S_{1D}\left(\frac{\psi}{\Delta\psi}\right) S_{1D}\left(\frac{\theta}{\Delta\theta}\right) S_{1D}\left(\frac{\alpha}{\Delta\alpha}\right), \tag{19}$$

with S_{1D} being the first-order b-spline function given by

$$S_{1D}(x) = \begin{cases} 1 - |x| & : |x| \le 1 \\ 0 & : |x| > 1 \end{cases}, \tag{20}$$

(then the deposition corresponds to a linear interpolation). In this work, the marker distribution function g is chosen as $g = f_{i0} N_p / (V_s n_{i0})$, where V_s the spatial volume of the computational box.

After solving the field equation for $\delta\Phi$, the spatial differential of $\delta\Phi$ is performed in the field-line-following coordinates to determine the perturbed electric field. The deposition and field solving are done in field-line-following coordinates because this coordinate system is efficient for resolving ITG modes, which have $k_\parallel \ll k_\perp$, where $k_\parallel$ and $k_\perp$ are the parallel and perpendicular wave-number, respectively.

5. Simulation results of linear and nonlinear ITG instabilities

In order to benchmark the results against those of Ref. [19], we adopt the DIII-D cyclone base case[29], which is a concentric-circular magnetic configuration. The main parameters used in the benchmarking are summarized in Table. 1.

Table 1. DIII-D cyclone base case parameters[29]. The safety factor profile is given by $q(r) = q_0 + (r - r_0)q'(r_0)$ with $q'(r_0) = \hat{s}q_0/r_0$, where $\hat{s}$ is the magnetic shear at $r = r_0$ (the radial center of the simulation box). In this case $R_0/\rho_i = 450.5$, where $\rho_i = v_{ti}/\Omega_i$ is the thermal ion gyro-radius at the magnetic axis, $v_{ti} = \sqrt{T_{i0}/m_i}$, $\Omega_i = B_{\text{axis}} q_i / m_i$ is the ion cyclotron angular frequency at the magnetic axis. Deuterium plasma is assumed in our simulation.

R_0	a	B_{axis}	q_0	$\hat{s}$	r_0	$\kappa_{T_i} R_0$	$\kappa_{n_i} R_0$	T_{i0}	$q_i T_{i0}/(eT_{e0})$
$1.32m$	$0.48m$	$1.91T$	1.40	0.78	$0.24m$	6.9	2.2	1.5keV	1

Although the DIII-D cyclone equilibrium is analytic and circular, the equilibrium is read in as a general equilibrium specified numerically in the G-EQDSK format of EFIT code. No analytic relations particular to this specific configuration is relied on.

Preprints (www.preprints.org) | NOT PEER-REVIEWED | Posted: 27 March 2018 doi:10.20944/preprints201803.0221.v1

Peer-reviewed version available at *plasma* **2018**, *1*, 10; doi:10.3390/plasma1010010

The radial center of the simulation box is at $r = r_0 = 0.24m$ and the radial width $\Delta r = 0.11m$, which is about $37.5\rho_i$. The perturbed potential $\delta\Phi$ is set to zero at the radial boundaries. When a marker moves out of the radial boundary, its vertical location is changed from Z to $-Z$ (this is to follow the drift orbit) and its weight is set to zero, where Z is the vertical coordinate of cylindrical coordinates. Figure. 2 shows the time evolution of an $n = 29$ linear ITG instability for DIII-D cyclone base case parameters. Clear exponential growth of the instability is observed. The frequency and growth rate in this case are $\omega_r/\Omega_i = 2.388 \times 10^{-3}$ and $\gamma/\Omega_i = 5.8 \times 10^{-4}$ while the corresponding results from Ref. [19] are $\omega_r/\Omega_i = 2.423 \times 10^{-3}$ and $\gamma/\Omega_i = 6.0 \times 10^{-4}$.

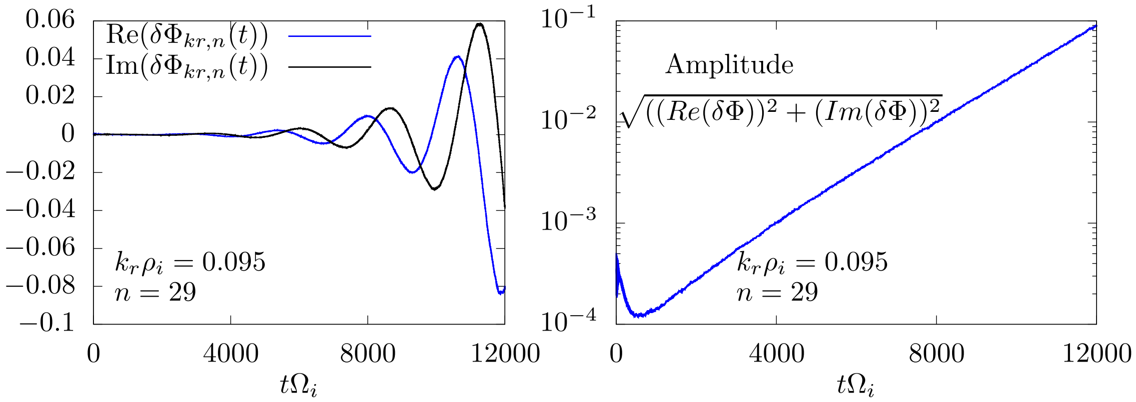

Figure 2. Time evolution of an $n = 29$ linear ITG instability for DIII-D cyclone base case parameters. In the simulation, the perturbed electric potential $\delta\Phi$ is Fourier filtered along the toroidal direction to retain only the $n = 29$ harmonic, which is further sine transformed along the radial direction and only low radial harmonics are retained. Shown here is the fundamental radial harmonic of $\delta\Phi$ near the low-field-side midplane, which corresponds to $k_r\rho_i = 0.095$. $\delta\Phi$ is normalized by T_e/e. The frequency and growth rate in this case are $\omega_r/\Omega_i = 2.388 \times 10^{-3}$ and $\gamma/\Omega_i = 5.8 \times 10^{-4}$, which correspond to the fifth data point in Fig. 4, where the corresponding results from Ref. [19] are $\omega_r/\Omega_i = 2.423 \times 10^{-3}$ and $\gamma/\Omega_i = 6.0 \times 10^{-4}$.

This is a multi-scale simulation, which includes both the slow-scale ITG instability and the fast-scale wave associated with the ion gyro-motion. In the simulation, we can identify the existence of the ion Bernstein wave (IBW) associated with the ion gyro-motion. The IBW is hidden in the simulation in Fig. 2, the details of which are plotted in Fig. 3(a) for $t\Omega_i = [0 : 200]$. The corresponding frequency spectrum is plotted in Fig 3(b), which shows a clear peak near the ion gyro-frequency.

Numerical parameters used in obtaining the above and the following results are as follows: the time step $\Delta t\Omega_i = 0.2$, the spatial resolution in (ψ, θ, α) is $(162, 64, 32)$, where the toroidal range is a wedge with $\Delta\alpha = 2\pi/n$, the number of total markers $N_p = 6.4 \times 10^6$ (the number of markers per cell is about 19). Increasing the number of markers to $N_p = 9.6 \times 10^6$ produced no significant difference in the real frequency or growth rate.

The code uses one dimensional domain decomposition along θ and 4 MPI processes are used for particle parallelization for each θ cell (the particle parallelization will be entirely replaced by OpenMP in near future) and thus total $64 \times 4 = 256$ MPI processes are used. The code run on NERSC Cori system and typical runs use eight Intel Xeon "Haswell" nodes, each of which is equipped with 32 physical cores supporting 2 hyper-threads and thus $2 \times 32 = 64$ logical cores. The code uses OpenMP to make use of this hyper-threading capability. For the above run with 6×10^4 time-steps, the wall-time is 2.3 hours. (Each Cori node has two sockets and each socket is populated with a 16-core Intel® Xeon$^{\mathrm{TM}}$ Processor E5-2698 v3 at 2.3 GHz.)

Peer-reviewed version available at plasma 2018, 1, 10; doi:10.3390/plasma1010010

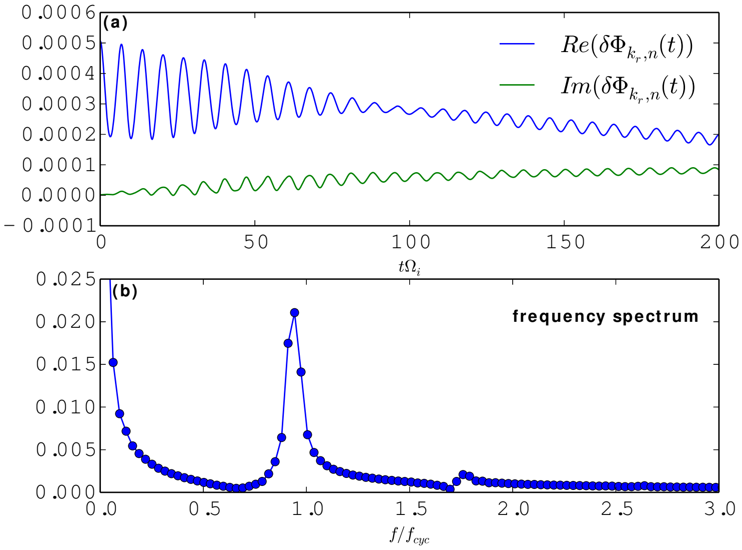

Figure 3. Time evolution (a) of the electric potential during $t\Omega_i = [0:200]$ and the corresponding frequency spectrum (b), which shows a clear peak near the ion gyro-frequency. Here $f_{\text{cyc}} = 2\pi/\Omega_i$.

Figure 4 presents the dependence of the linear ITG mode frequency and growth rate on the ion temperature gradient κ_{T_i}, which shows that both the frequency and growth rate increase with the temperature gradient drive. Also plotted in Fig. 4 are the fully kinetic results from Ref. [19], which are in good agreement with our new results.

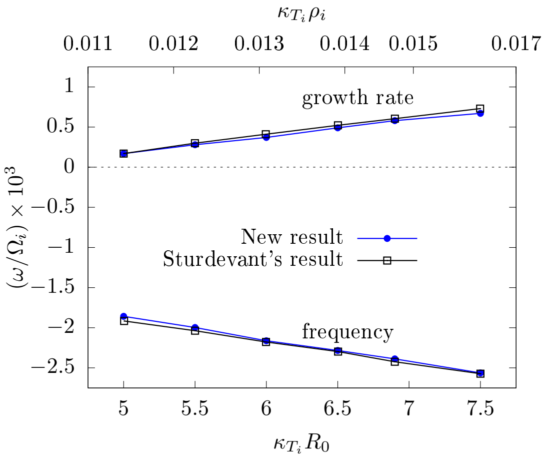

Figure 4. Dependence of ITG mode frequency and growth rate on the ion temperature gradient κ_{T_i} for the DIII-D cyclone base case. The upper horizontal axis shows the ion temperature gradient normalized by the thermal ion gyro-radius. Also plotted are the results from Ref. [19], which are in good agreement with our new results.

Gyrokinetic simulations found that ITG instabilities usually reach peak growth rate near $k_\theta\rho_i \approx 0.3$, where k_θ is the bi-normal wave-number $k_\theta \approx nq_0/r_0$. This trend can also be captured by the fully kinetic ion model. Figure 5 shows the dependence of ITG growth rate and frequency on $k_\theta\rho_i$ given by the fully kinetic model, which shows that the growth rate reaches a peak near $k_\theta\rho_i \approx 0.4$. Also plotted in Fig. 5 are the gyrokinetic results from Ref. [30] and [29], which agree with our results within an acceptable discrepancy.

Peer-reviewed version available at *plasma* **2018**, *1*, 10; doi:10.3390/plasma1010010

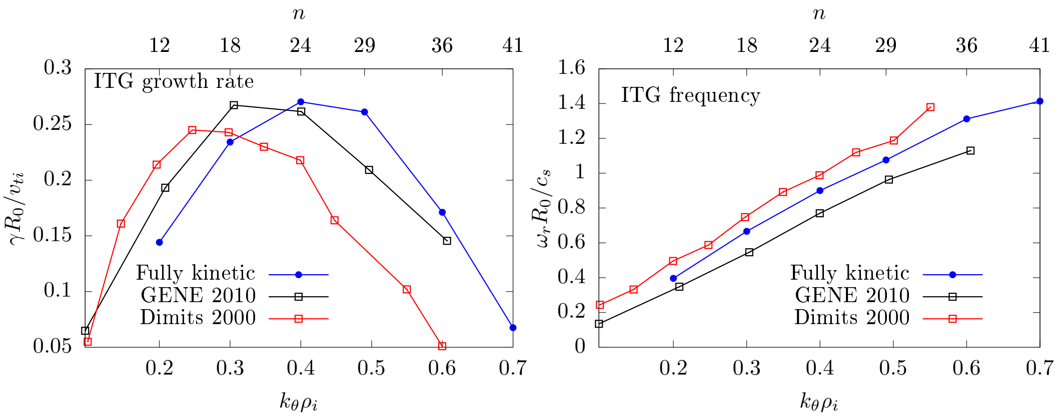

Figure 5. Dependence of ITG mode growth rate and frequency on $k_\theta \rho_i$ for DIII-D cyclone base case. The upper horizontal axis shows the corresponding toroidal mode number n. Also plotted are the gyrokinetic results reported in Ref. [30] and [29]. Several factors may contribute to the difference between the three results. In our case $\rho_i = R_0/450.5$, while $\rho_i = R_0/500.0$ in Ref [30]. Safety factor profiles are slightly different: $q(r) = q_0 + (r - r_0)q'(r_0)$ in this work, while $q(r) = 0.86 - 0.16r/a + 2.52(r/a)^2$ in Ref. [30] and q profile variation is neglected in the flux-tube model of Ref. [29]. Deuterium plasma is used in our simulation.

Figure 6 plots the two-dimensional mode structure of the $n = 29$ ITG instability in the poloidal plane, which shows a clear ballooning structure (i.e., the amplitude on the low-field-side is larger than that on the high-field-side). This is consistent with the physical picture that ITG instabilities are driven by the $E \times B$ drift on the tokamak low-field-side while the $E \times B$ drift on the high-field side (the "good-curvature" side) suppresses the instabilities.

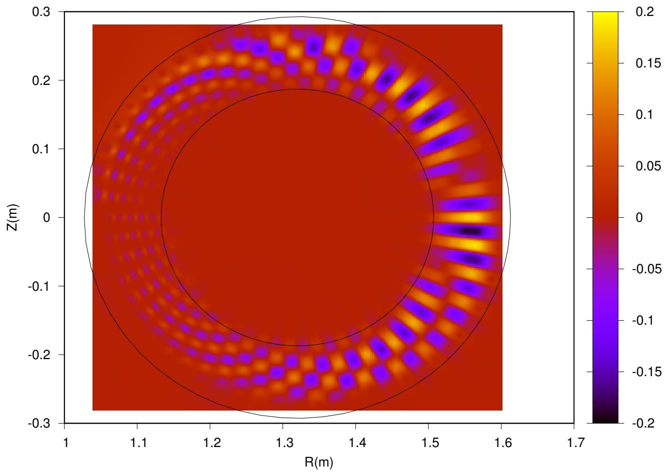

Figure 6. Mode structure of the $n = 29$ ITG instability in the poloidal plane. Plotted here is the perturbed electric potential $\delta\Phi$ at $t\Omega_i = 12000$.

We furthermore extend the work in Ref [19] to the nonlinear regime and investigate the nonlinear saturation of the ITG instability. Figure 7 plots the nonlinear evolution of the $n = 29$ ITG instability, which shows that after the linear growth stage, the mode amplitude saturates and then is suppressed. This suppression is due to the $E \times B$ trapping effect[18]. We are also studying the nonlinear interaction between ITG modes of multiple toroidal mode numbers and their coupling to the zonal flow, which will be reported in a future publication.

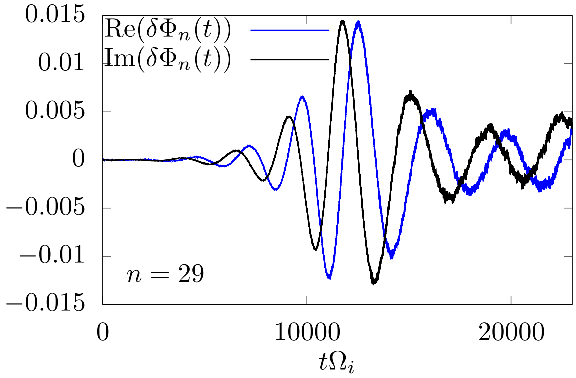

Figure 7. Nonlinear saturation of the $n = 29$ ITG instability in the DIII-D cyclone base case. The perturbed potential $\delta\Phi$ (normalized by T_e/e) is measured on the low-field-side midplane and averaged over the radial domain.

6. Summary

The viability of the fully kinetic ion model in simulating the low-frequency ITG instability in tokamaks is demonstrated in this work by using a simple full orbit integrator. This work also extends the previous work from analytic circular magnetic equilibria to general magnetic equilibria, enabling simulation of realistic equilibria reconstructed from tokamak experiments. We also extend the previous work from the linear regime to nonlinear regime and present preliminary results on the nonlinear saturation of the ITG instability.

The Fortran code used in obtaining the results presented in this work is released as an open-source software under the GNU General Public License v3.0. The source code can be downloaded from: https://github.com/Youjunhu/Fully_kinetics_tokamak_ITG.

Acknowledgments: Y. Hu thanks Benjamin Sturdevant, Junyi Cheng, Yichen Fu, Lei Ye, and Baolong Hao for useful discussions. This work is supported by the U.S. Department of Energy, Office of Fusion Energy Sciences under Award Nos. DE-SC0008801 and DE-FG02-08ER54954. This research used resources of the National Energy Research Scientific Computing Center, a DOE Office of Science User Facility supported by the Office of Science of the U.S. Department of Energy under Contract No. DE-AC02-05CH11231.

Author Contributions: S. Parker and Y. Chen conceived the idea of full ion kinetics for low-frequency ITG instabilities and developed the physical and numerical model; Y. Hu implemented the numerical model for the linear ITG instabilities, analyzed the results, and wrote the paper. M. Miecnikowski developed the nonlinear ITG model and analyzed the results.

Conflicts of Interest: The authors declare no conflict of interest. The founding sponsors had no role in the design of the study; in the collection, analyses, or interpretation of data; in the writing of the manuscript, and in the decision to publish the results.

Appendix. Electromagnetic model for ITG instabilities with drift-kinetic electrons

We are working on extending the fully kinetic ion model for ITG instabilities to the electromagnetic case with drift-kinetic electrons. This model was first introduced in Ref. [31]. In this model, Faraday's law is discretized using the following second-order implicit scheme (Crank–Nicolson method):

$$\frac{\delta\mathbf{B}^{(n+1)} - \delta\mathbf{B}^{(n)}}{\Delta t} = -\nabla \times \left(\frac{\delta\mathbf{E}^{(n+1)} + \delta\mathbf{E}^{(n)}}{2} \right), \tag{A1}$$

where Δt is the time-step, the superscript n stands for the current step, $n+1$ for the future step. With the displacement current dropped, Ampère's law is written

$$\mu_0^{-1}\nabla \times \delta\mathbf{B}^{(n+1)} = \delta\mathbf{J}_i^{(n+1)} + \delta\mathbf{J}_e^{(n+1)}, \tag{A2}$$

Peer-reviewed version available at *plasma* **2018**, *1*, 10; doi:10.3390/plasma1010010

where μ_0 is the permeability of free space, $\delta\mathbf{J}_i$ and $\delta\mathbf{J}_e$ are the perturbed ion and electron current, respectively. The perturbed perpendicular electron current $\delta\mathbf{J}_{e\perp}$ is given by the drift-kinetic approximation:

$$\delta\mathbf{J}_{e\perp} = \underbrace{-\frac{en_{e0}}{B_0}\delta\mathbf{E}\times\mathbf{b}}_{E\times B\text{ flow}} + \underbrace{\frac{1}{B_0}\mathbf{b}\times\nabla\delta p_{\perp e}}_{\text{diamagnetic flow}}, \tag{A3}$$

where $\delta p_{\perp e}$ is the perturbed perpendicular electron pressure, which is computed by using the drift-kinetic δf PIC method. The ion response $\delta\mathbf{J}_i$ is computed by using the implicit fully kinetic δf PIC method discussed in Sec. 3 with magnetic perturbations retained. Equations (A1) and (A2) serves as the field equation for $\delta\mathbf{E}^{(n+1)}$ and $\delta\mathbf{B}^{(n+1)}$ and are solved as a coupled system in the field-line-following coordinates. This model is being developed. All the results reported in this paper are obtained by using the code being developed and taking the electrostatic limit and using adiabatic electrons (i.e., the model described in Sec. 2.1).

References

1. Guzdar, P.N.; Chen, L.; Tang, W.M.; Rutherford, P.H. Ion-temperature-gradient instability in toroidal plasmas. *The Physics of Fluids* **1983**, *26*, 673–677, [http://aip.scitation.org/doi/pdf/10.1063/1.864182].
2. Rettig, C.L.; Rhodes, T.L.; Leboeuf, J.N.; Peebles, W.A.; Doyle, E.J.; Staebler, G.M.; Burrell, K.H.; Moyer, R.A. Search for the ion temperature gradient mode in a tokamak plasma and comparison with theoretical predictions. *Physics of Plasmas* **2001**, *8*, 2232–2237, [https://doi.org/10.1063/1.1362537].
3. Lin, Z.; Hahm, T.S.; Lee, W.W.; Tang, W.M.; White, R.B. Turbulent Transport Reduction by Zonal Flows: Massively Parallel Simulations. *Science* **1998**, *281*, 1835–1837.
4. Xie, H.S.; Xiao, Y.; Lin, Z. New Paradigm for Turbulent Transport Across a Steep Gradient in Toroidal Plasmas. *Phys. Rev. Lett.* **2017**, *118*, 095001.
5. Parker, S.E.; Lee, W.W.; Santoro, R.A. Gyrokinetic simulation of ion temperature gradient driven turbulence in 3D toroidal geometry. *Phys. Rev. Lett.* **1993**, *71*, 2042–2045.
6. Idomura, Y.; Tokuda, S.; Kishimoto, Y. Global gyrokinetic simulation of ion temperature gradient driven turbulence in plasmas using a canonical Maxwellian distribution. *Nuclear Fusion* **2003**, *43*, 234.
7. Gao, Z.; Sanuki, H.; Itoh, K.; Dong, J.Q. Short wavelength ion temperature gradient instability in toroidal plasmas. *Physics of Plasmas* **2005**, *12*, 022502, [https://doi.org/10.1063/1.1840687].
8. Chen, Y.; Parker, S.E. Electromagnetic gyrokinetic δf particle-in-cell turbulence simulation with realistic equilibrium profiles and geometry. *Journal of Computational Physics* **2007**, *220*, 839 – 855.
9. Ye, L.; Xu, Y.; Xiao, X.; Dai, Z.; Wang, S. A gyrokinetic continuum code based on the numerical Lie transform (NLT) method. *Journal of Computational Physics* **2016**, *316*, 180 – 192.
10. Görler, T.; Lapillonne, X.; Brunner, S.; Dannert, T.; Jenko, F.; Merz, F.; Told, D. The global version of the gyrokinetic turbulence code GENE. *Journal of Computational Physics* **2011**, *230*, 7053 – 7071.
11. Ku, S.; Chang, C.; Diamond, P. Full-f gyrokinetic particle simulation of centrally heated global ITG turbulence from magnetic axis to edge pedestal top in a realistic tokamak geometry. *Nuclear Fusion* **2009**, *49*, 115021.
12. Chang, C.S.; Ku, S.; Tynan, G.R.; Hager, R.; Churchill, R.M.; Cziegler, I.; Greenwald, M.; Hubbard, A.E.; Hughes, J.W. Fast Low-to-High Confinement Mode Bifurcation Dynamics in a Tokamak Edge Plasma Gyrokinetic Simulation. *Phys. Rev. Lett.* **2017**, *118*, 175001.
13. Lin, Y.; Wang, X.Y.; Chen, L.; Lu, X.; Kong, W. An improved gyrokinetic electron and fully kinetic ion particle simulation scheme: benchmark with a linear tearing mode. *Plasma Physics and Controlled Fusion* **2011**, *53*, 054013.
14. Waltz, R.E.; Deng, Z. Nonlinear theory of drift-cyclotron kinetics and the possible breakdown of gyro-kinetics. *Physics of Plasmas* **2013**, *20*, 012507, [https://doi.org/10.1063/1.4773039].
15. Kramer, G.J.; Budny, R.V.; Bortolon, A.; Fredrickson, E.D.; Fu, G.Y.; Heidbrink, W.W.; Nazikian, R.; Valeo, E.; Zeeland, M.A.V. A description of the full-particle-orbit-following SPIRAL code for simulating fast-ion experiments in tokamaks. *Plasma Physics and Controlled Fusion* **2013**, *55*, 025013.

16. Kuley, A.; Lin, Z.; Bao, J.; Wei, X.S.; Xiao, Y.; Zhang, W.; Sun, G.Y.; Fisch, N.J. Verification of nonlinear particle simulation of radio frequency waves in tokamak. *Physics of Plasmas* **2015**, *22*, 102515, [https://doi.org/10.1063/1.4934606].
17. Sturdevant, B.J.; Parker, S.E.; Chen, Y.; Hause, B.B. An implicit δf particle-in-cell method with sub-cycling and orbit averaging for Lorentz ions. *Journal of Computational Physics* **2016**, *316*, 519 – 533.
18. Miecnikowski, M.T.; Sturdevant, B.J.; Chen, Y.; Parker, S.E. Nonlinear saturation of the slab ITG instability and zonal flow generation with fully kinetic ions. *Physics of Plasmas* **2018**, *25*, 055901, [https://doi.org/10.1063/1.5011681].
19. Sturdevant, B.J.; Chen, Y.; Parker, S.E. Low frequency fully kinetic simulation of the toroidal ion temperature gradient instability. *Physics of Plasmas* **2017**, *24*, 081207, [https://doi.org/10.1063/1.4999945].
20. Birdsall, C.; Langdon, A. *Plasma Physics via Computer Simulation*; CRC Press, 2004.
21. Parker, S.E.; Lee, W.W. A fully nonlinear characteristic method for gyrokinetic simulation. *Physics of Fluids B: Plasma Physics* **1993**, *5*, 77–86, [https://doi.org/10.1063/1.860870].
22. Aydemir, A.Y. A unified Monte Carlo interpretation of particle simulations and applications to non-neutral plasmas. *Physics of Plasmas* **1994**, *1*, 822–831, [https://doi.org/10.1063/1.870740].
23. Süli, E.; Mayers, D.F. *An Introduction to Numerical Analysis*; Cambridge University Press, 2003.
24. Qin, H.; Zhang, S.; Xiao, J.; Liu, J.; Sun, Y.; Tang, W.M. Why is Boris algorithm so good? *Physics of Plasmas* **2013**, *20*, 084503.
25. Parker, S.; Birdsall, C. Numerical error in electron orbits with large $\omega_{ce}\Delta t$. *Journal of Computational Physics* **1991**, *97*, 91 – 102.
26. Lao, L.; John, H.S.; Stambaugh, R.; Kellman, A.; Pfeiffer, W. Reconstruction of current profile parameters and plasma shapes in tokamaks. *Nucl. Fusion* **1985**, *25*, 1611.
27. Beer, M.A.; Cowley, S.C.; Hammett, G.W. Field-aligned coordinates for nonlinear simulations of tokamak turbulence. *Phys. Plasmas (1994-present)* **1995**, *2*, 2687–2700.
28. Chen, Y.; Parker, S.E. A delta-f particle method for gyrokinetic simulations with kinetic electrons and electromagnetic perturbations. *Journal of Computational Physics* **2003**, *189*, 463 – 475.
29. Dimits, A.M.; Bateman, G.; Beer, M.A.; Cohen, B.I.; Dorland, W.; Hammett, G.W.; Kim, C.; Kinsey, J.E.; Kotschenreuther, M.; Kritz, A.H.; Lao, L.L.; Mandrekas, J.; Nevins, W.M.; Parker, S.E.; Redd, A.J.; Shumaker, D.E.; Sydora, R.; Weiland, J. Comparisons and physics basis of tokamak transport models and turbulence simulations. *Physics of Plasmas* **2000**, *7*, 969–983, [https://doi.org/10.1063/1.873896].
30. Lapillonne, X.; McMillan, B.F.; Görler, T.; Brunner, S.; Dannert, T.; Jenko, F.; Merz, F.; Villard, L. Nonlinear quasisteady state benchmark of global gyrokinetic codes. *Physics of Plasmas* **2010**, *17*, 112321, [https://doi.org/10.1063/1.3518118].
31. Chen, Y.; Parker, S.E. Particle-in-cell simulation with Vlasov ions and drift kinetic electrons. *Phys. Plasmas* **2009**, *16*, 052305.